

Journal of Mechanics of Materials and Structures

**NETWORK EVOLUTION MODEL OF ANISOTROPIC STRESS
SOFTENING IN FILLED RUBBER-LIKE MATERIALS: PARAMETER
IDENTIFICATION AND FINITE ELEMENT IMPLEMENTATION**

Roozbeh Dargazany, Vu Ngoc Khiêm, Uwe Navrath and Mikhail Itskov

Volume 7, No. 8-9

October 2012



NETWORK EVOLUTION MODEL OF ANISOTROPIC STRESS SOFTENING IN FILLED RUBBER-LIKE MATERIALS: PARAMETER IDENTIFICATION AND FINITE ELEMENT IMPLEMENTATION

ROOZBEH DARGAZANY, VU NGOC KHIÊM, UWE NAVRATH AND MIKHAIL ITSKOV

A purely micromechanical network evolution theory granting new insight into the damage mechanism was proposed previously by the authors (Dargazany and Itskov, 2009). In this follow-up paper, we further formulate the network evolution model for implementation into finite element simulations. To this end, a general internal variable formulation is developed which determines the inelastic response of the microstructure on the basis of the free energy function. The thermodynamical consistency of the network evolution model is then verified analytically. Next, the predictive capabilities of the model are demonstrated by means of several experiments especially designed to capture stress softening, permanent set, and induced anisotropy. Finally, the influence of the filler concentration on material parameters is studied.

1. Introduction

Constitutive modeling of the macroscopic behavior of rubber-like materials has long been the subject of interest; see [Treloar 2005] or [Mark and Erman 2007] for an introduction. In the behavior of rubbers, hyperelasticity and stress softening are the most studied phenomena.

Investigations of inelastic effects in rubber materials, as, for example, stress softening, date back to the beginning of the last century, starting with [Bouasse and Carrière 1903; Holt 1932]. Later, Mullins and his coworkers investigated rubber-like materials in detail and reported different inelastic features of filled rubbers [Mullins and Tobin 1957; 1965], which still can hardly be modeled micromechanically.

Bueche [1960; 1961] associated the Mullins effect with the breakage of weak bonds between polymer chains and filler particles (see [Aksel and Hübner 1996]). This assumption was redefined by some authors as the slippage of polymer chains on filler clusters [Houwink 1956; Killian et al. 1994]. This concept has been further developed by describing the chain entanglements between particles [Hamed and Hatfield 1989] and has consequently been employed as a basis for the thermodynamical representation of continuum damage mechanics [Simo 1987; Miehe and Keck 2000]. Following the lead of Bueche, Govindjee and Simo [1991; 1992] decomposed the rubber matrix into a pure rubber network and a polymer-filler network, the latter being subjected to damage. The model was based on the isotropic three-chain model [James and Guth 1943], in which the damage depends on the largest principal stretch. The main assumption of their model is that damage takes place only in the presence of fillers. Indeed, recent experiments show that only filled elastomers that can crystallize show stress softening [Diani et al. 2009].

Rajagopal and Wineman [1992] developed a set of integral-type constitutive equations governing the microstructural damage induced by the rupture of molecular bonds and recreation of new ones. Based

Keywords: Mullins effect, stress softening, constitutive behavior, microstructures, anisotropic material, rubber material.

on this approach, stress softening and permanent set in some applications were calculated based on a neo-Hookean-type model [Huntley et al. 1996]. Using a similar technique, Demirkoparan et al. [2009] generalized the two-reference configuration theory proposed in [Wineman and Rajagopal 1990] to fibrous soft matter by considering the material as a composition of two components, in which the microstructure change only occurs in the fibrous component. The resulting model was able to capture stress softening and permanent set in fibrous materials.

By categorizing polymer chains into two types, flexed and extended, Drozdov and Dorfmann [2001] developed a micromechanically motivated model that can take stress softening and permanent set into account.

Based on the concept of pseudoelasticity, Dorfmann and Ogden [2004] proposed a phenomenological approach to account for permanent set. Combining the three-chain [James and Guth 1943] and eight-chain [Arruda and Boyce 1993] models, Elías-Zúñiga and Beatty [2002] proposed a model that successfully predicted the constitutive behavior of rubber under multiaxial loading conditions. The model had a relatively simple formulation and only three model parameters. Next, by redistributing of the representative chains in all possible orientations, the full network model was attained [Beatty 2003]. In another approach, Elías-Zúñiga and Rodríguez [2010] proposed a phenomenological damage function and substituted it into the non-Gaussian full-network model. The final model showed good agreement with experimental results on equibiaxial tension tests.

Hanson et al. [2005] associated the anisotropic Mullins effect with the removal of the chain entanglements during slippage of chains on each other. Thus, despite the constant number of active chains, the density of entanglements changes under deformation.

In order to describe the anisotropic Mullins effect, the idea of network decomposition of [1991] was exploited by Göktepe and Miehe [2005]. They further presented a microsphere model with 21 material directions instead of the three principal directions proposed by Govindjee and Simo [1991; 1992]. By considering nonaffinity in the polymer–polymer network, the developed model is also efficient for unfilled elastomers. Zimmermann and Wineman [2005] derived the constitutive theories that characterize the implications of polymer chains debonding on the mechanical properties of the rubber matrix, particularly induced anisotropy, and permanent set.

In another approach, Diani et al. [2006] further generalized the one-dimensional network alteration model into a three-dimensional model. Then, by proposing a phenomenological damage function, the losses of energy in different directions were taken into account. The so-obtained model was then compared with quasistatic experiments and agreed well with the measured residual strain and induced anisotropy.

In [Dargazany and Itskov 2009], we proposed a micromechanical constitutive model for carbon black filled rubber-like materials, which can describe such anisotropic inelastic phenomena as the Mullins effect, permanent set, and induced anisotropy. The model is based on the idea of network decomposition of [Govindjee and Simo 1991], where the rubber network is decomposed into a pure rubber network and a polymer-filler network. Damage in the polymer-filler network is considered as a consequence of chain sliding on or debonding from aggregates. In contrast to previous works on anisotropy of the Mullins effect, no phenomenological damage function is introduced. Damage in different directions is governed by a network evolution concept which describes changes in the interaggregate distribution of polymer

chains. The proposed model demonstrates very good agreement with experimental data with respect to the above-mentioned inelastic effects, although it considers filler aggregates as rigid bodies.

Moreover, the model benefits from its simplicity, small number of physically motivated material parameters, and fast fitting procedure. However, the predictions of the model were validated by only one set of experimental data and, furthermore, the thermodynamical consistency and implementation procedure of the model into finite element code were not discussed. Addressing these issues is the main goal of this work.

The paper is organized as follows. The fundamentals of the network evolution model are reviewed in Section 2. Then, the constitutive modeling approach is discussed in Section 3. In Section 4, the thermodynamical consistency of the model is studied and verified analytically. In order to implement the network evolution model into finite element simulations, the tangent tensor is derived using a linearization procedure discussed in Section 5. Section 6 describes the experimental procedure which is used later in Section 7 for evaluation of the material parameters. The implementation of the proposed constitutive model into commercial FE code (ABAQUS) is presented in Section 8. Finally, the Appendix provides details of the derivation of the tangent tensor.

2. Network evolution model

2.1. Statistical mechanics of a single chain. According to Gaussian statistics, the probability that a segment of a freely rotating chain with n segments and end-to-end distance R exists is given by

$$P_G(n, R) dR = \sqrt{\frac{\alpha'}{\pi n l^2}} \exp\left(-\frac{\alpha' R^2}{n l^2}\right) dR, \quad (1)$$

where l denotes the segment length and $\alpha' = \frac{3}{2}(1 - \cos \theta)/(1 + \cos \theta)$ is expressed in terms of the supplement to the valence angle $\theta = 70.5^\circ$. Accordingly, the probability of existence of a polymer chain connecting two constrained segments, so that none of the segments between numbers 1 and n is joined to an aggregate surface, is given by (see [Dargazany and Itskov 2009])

$$P(n, \bar{R}) = \kappa \sqrt{\frac{\alpha'}{\pi n}} \exp A, \quad \text{with} \quad (2)$$

$$A = -\alpha' \frac{\bar{R}^2}{n} - \kappa \sqrt{\frac{\alpha'}{\pi}} \left[2\sqrt{n} \exp\left(-\alpha' \frac{\bar{R}^2}{n}\right) + 2\bar{R} \sqrt{\pi \alpha'} \left(\operatorname{erf}\left(\bar{R} \sqrt{\frac{\alpha'}{n}}\right) - \operatorname{erf}(\bar{R} \sqrt{\alpha'}) \right) - 2 \exp(-\alpha' \bar{R}^2) \right],$$

where κ denotes the average area of active adsorption sites available for one bond.

(A bar over a parameter denotes its normalized value with respect to the segment length l : thus $\bar{R} = R/l$, and so on.)

Let us denote the vectors connecting the two ends of the chain in the reference and deformed configurations by \mathbf{R} and \mathbf{r} , and their lengths by R and r , respectively. Accordingly, one has

$$\mathbf{r} = \mathbf{F}_m \mathbf{R}, \quad r = \overset{D}{\lambda} R, \quad (3)$$

where \mathbf{F}_m denotes the deformation gradient at the microscale, and $\overset{D}{\lambda} = \sqrt{\mathbf{D} \mathbf{F}_m^T \mathbf{F}_m \mathbf{D}}$ the microstretch in the direction specified by the unit vector \mathbf{D} . Hereafter, the following font styles are used: for a scalar X , a vector \mathbf{X} , a second-order tensor \mathbf{X} , and a fourth-order tensor \mathbb{X} .

Based on non-Gaussian statistics, the strain energy density of a freely rotating chain is written as

$$\psi_c(n, \bar{r}) = bnKT \left(\frac{\bar{r}}{abn} \beta + \ln \frac{\beta}{\sinh \beta} \right), \quad (4)$$

where the coefficients a and b are calculated by [Treloar 2005]

$$a = \frac{3}{2\alpha'} \cos^{-1} \left(\frac{\theta}{2} \right), \quad b = \frac{2}{3} \alpha' \cos^2 \left(\frac{\theta}{2} \right), \quad (5)$$

and $\beta = \mathcal{L}^{-1}(\bar{r}/abn)$ is expressed in terms of the inverse Langevin function \mathcal{L}^{-1} , while K and T denote Boltzmann's constant and the absolute temperature.

2.2. Strain energy of the rubber matrix. By considering rubber as a nearly incompressible material, its strain energy function $\Psi_N(\mathbf{C})$ can be decoupled into isochoric and volumetric parts by (see, for example, [Holzapfel 2000])

$$\Psi_N(\mathbf{C}) = \Psi_M(\bar{\mathbf{C}}) + U(J), \quad (6)$$

where \mathbf{C} denotes the right Cauchy–Green tensor, $J^2 = \det \mathbf{C}$, and $\bar{\mathbf{C}} = J^{-2/3} \mathbf{C}$.

The rubber matrix is then decomposed into a pure rubber network (CC) and a polymer-filler network (PP) which act parallel to each other (for details see [Dargazany and Itskov 2009]). Accordingly, the isochoric strain energy of the rubber matrix Ψ_M can be represented as

$$\Psi_M = \Psi_{cc} + \Psi_{pp}, \quad (7)$$

where Ψ_{cc} and Ψ_{pp} denote the strain energies of the CC and PP networks per unit reference volume of the material (see Figure 1).

2.3. Pure rubber network. The pure rubber network is considered as an ideally elastic network with affine motion of cross-links and identical chains that are initially in the unperturbed state, in which the mean end-to-end distance of a freely rotating chain is $R_0 = a\sqrt{bn}$. Accordingly, the entropic energy of a single chain subjected to elongation is represented by

$$\psi(n, \frac{d}{\chi}) := \psi_c(n, \frac{d}{\lambda} \bar{R}_0), \quad (8)$$

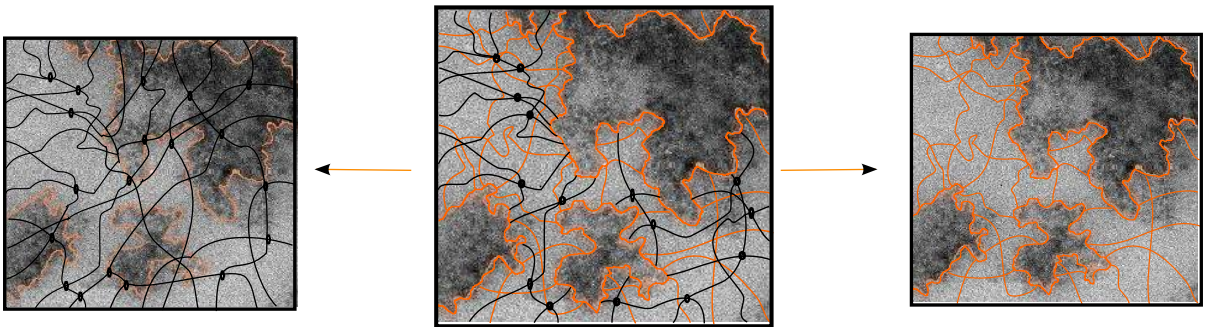


Figure 1. Illustration of the network decomposition concept.

where we keep in mind that in the CC network the microstretch $\overset{D}{\lambda}$ is equal to the macrostretch $\overset{D}{\chi}$. In order to obtain the strain energy of the CC network, N_c chains with n_c segments are considered in each spatial direction, so that

$$\Psi_{cc} = \frac{1}{A_s} \int_S N_c \psi(n_c, \overset{D}{\chi}) d\overset{D}{u}, \tag{9}$$

where A_s represents the surface area of the microsphere S , and $d\overset{D}{u}$ the unit area of the surface with the normal direction \mathbf{D} .

2.4. Polymer-filler network. The evolution of the polymer-filler network is assumed to be responsible for the already mentioned stress softening. Let $\tilde{N}(n, \bar{r})$ be the number of chains with number of segments (relative length) n , relative end-to-end distance \bar{r} , and end-to-end direction specified by the unit vector \mathbf{D} . The integration over the whole set D_A of relative chain lengths n available in the direction \mathbf{D} further yields the free energy of chains in this direction as

$$\overset{D}{\Psi} = \int_{D_A} \tilde{N}(n, \bar{r}) \psi_c(n, \bar{r}) dn. \tag{10}$$

The network evolution was described as an interaction of two simultaneous processes of aggregate-polymer debonding and network rearrangement. In the course of deformation, polymer chains begin to slide on or debond from the aggregates. This debonding starts with the shortest chain and gradually involves longer and longer chains. Under unloading, the debonded chains do not reattach back to the aggregate’s active sites, and thus the maximal microstretch previously reached in the loading history,

$$\overset{D}{\lambda}_m = \max_{\tau \in (-\infty, t]} \overset{D}{\lambda}(\tau), \tag{11}$$

is crucial for the description of the polymer-filler debonding. Accordingly, the length of the shortest available chain in the deformed subnetwork is then obtained by (see also [Dargazany and Itskov 2009])

$$n_{c-f}(\overset{D}{\lambda}_m) = \frac{\nu \overset{D}{\lambda}_m \bar{R}}{ab}, \tag{12}$$

where $\nu > 1$ denotes a sliding ratio and is a material parameter.

Furthermore, we assume an upper limit for the length of a chain between two aggregates, denoted in the following by n_{\max} (for details see [Dargazany and Itskov 2009]). Accordingly, the set of available relative lengths of chains bonded to aggregates in the direction \mathbf{D} can be expressed by

$$D_A(\overset{D}{\lambda}_m) = \{n \mid n_{c-f}(\overset{D}{\lambda}_m) \leq n \leq n_{\max}\}. \tag{13}$$

By these means, the material behavior in the direction \mathbf{D} is influenced by the loading history.

The concept of chain rearrangement in a rubber network suggests that the detachment of chains from the aggregate surface does not necessarily result in the complete loss of their role in the network entropic energy, but it may also lead to the activation of some new segments. Thus, all in all, one can assume that the total number of active segments remains constant. This assumption yields

$$\tilde{N}(n, \bar{r}) = N_0 \Phi(\overset{D}{\lambda}_m) P(n, \bar{R}) = N_0 \Phi(\overset{D}{\lambda}_m) \hat{P}(n), \tag{14}$$

where

$$\Phi(x) = \left(\int_{D_A(x)} \hat{P}(n) n dn \right)^{-1}. \tag{15}$$

We consider \bar{R} as a material constant, and introduce the notation $\hat{P}(n) := P(n, \bar{R})$. The variable N_0 represents the number of active chains per unit undeformed volume, and will also be considered as a material parameter. Finally, considering (14) and (13) in (10), the energy of a subnetwork in direction \mathbf{D} is obtained as

$$\Psi^D = N_0 \Phi(\lambda_m^D) \int_{D_A(\lambda_m^D)} \hat{P}(n) \psi_c(n, \lambda^D \bar{R}) dn. \tag{16}$$

3. Constitutive modeling

3.1. Three-dimensional generalization. Assuming an isotropic spatial distribution of polymer chains in the rubber matrix, the macroscopic energy of a three-dimensional network can be written as

$$\Psi_{cc} = \frac{1}{A_s} \int_S N_c \psi(n_c, \lambda^D) d\mathbf{u}^D, \quad \Psi_{pp} = \frac{1}{A_s} \int_S \Psi^D d\mathbf{u}^D. \tag{17}$$

The integration is carried out numerically by

$$\Psi_{cc} \cong \sum_{i=1}^k N_c \psi(n_c, \lambda^{D_i}) w_i, \quad \Psi_{pp} \cong \sum_{i=1}^k \Psi^{D_i} w_i, \tag{18}$$

where w_i are weight factors corresponding to the collocation directions \mathbf{D}_i ($i = 1, 2, \dots, k$). As shown in [Ehret et al. 2010], the numerical scheme of [Heo and Xu 2001] demonstrates the least error in prediction of the induced anisotropy in comparison with the number of integration points and thus is used in this study. Accordingly, a set of $k = 45$ integration points on the half-sphere is chosen. Substitution of (16) into (18) yields the energy of the rubber matrix as

$$\Psi_M = \Psi_{cc} + \Psi_{pp} = \frac{\tilde{N}_c}{KT} \sum_{i=1}^k w_i \psi(n_c, \lambda^{D_i}) + \frac{\tilde{N}_0}{KT} \sum_{i=1}^k w_i \int_{D_A(\lambda_m^{D_i})} \Phi(\lambda_m^{D_i}) \hat{P}(n) \psi_c(n, \lambda^{D_i} \bar{R}) dn, \tag{19}$$

where

$$\tilde{N}_c = N_c KT, \quad \tilde{N}_0 = N_0 KT. \tag{20}$$

3.2. Strain amplification. In a filler-reinforced rubber network, the stretch of the polymer chains between aggregates (microstretch) generally exceeds the stretch applied to the rubber matrix (macrostretch). This strain amplification concept is based on the fact that filler aggregates are considerably stiffer than the polymer chains connecting them together [Rault et al. 2006]. This inhomogeneity of the material leads to the inhomogeneity in the microstretch distribution. Accordingly, the amplification function X is defined to establish a relationship between the microstretch λ^D and the macrostretch λ^D , and is written as

$$\lambda^D = X(\lambda^D) = \frac{\lambda^D - C^p}{1 - C^p}, \tag{21}$$

where $C \in (0, 1)$ represents the volume fraction of filler per unit volume of rubber matrix ($C < 0.3$ in most studies), and p depends on the structure of the filler network. Bueche [1961] showed that $p = \frac{1}{3}$ in the case of a statistically homogeneous distribution of spherical particles (see, for example, [Govindjee 1997; Bergström and Boyce 1999]).

The strain amplification concept is based on the following assumptions.

- (1) Filler aggregates are distributed and colonized randomly in three dimensions.
- (2) The stiffness of the rubber matrix is negligible in comparison to that of the filler aggregates, and thus the filler aggregates can be considered as rigid inclusions.
- (3) Changes in the aggregate's volume under deformation are negligible.
- (4) There is no energy dissipation in the aggregates.

Let us represent parameters related to fillers, polymers, additives, and the rubber matrix by subscript f , p , a , and r , respectively. Then

$$C = \frac{V_f}{V_r}, \quad V_r = V_f + V_p + V_a, \quad (22)$$

where V_\bullet denotes the volume. In industrial applications, the amount of filler in a rubber sample is given by C_f which denotes the mass parts of filler per hundred parts of rubber (phr):

$$C_f = \frac{M_f}{M_p} = \frac{V_f \rho_f}{V_p \rho_p}, \quad M_r = M_f + M_p + M_a, \quad (23)$$

where ρ_\bullet and M_\bullet represent the density and mass of the corresponding ingredients, respectively. The amount of additive, which is mainly composed of processing agents, can be considered to be around 5–10 phr. Accordingly, one can simply express C as

$$C = \frac{V_f/V_p}{V_f/V_p + 1 + M_a/(\rho_a V_p)} = \frac{C_f \rho_p/\rho_f}{(1 + 0.1 \rho_p/\rho_a) + C_f \rho_p/\rho_f}. \quad (24)$$

Note that (21) is valid as far as $\frac{p}{\chi} > C^p$, otherwise the deformation of aggregates should also be taken into account. Experimental results, however, show that the validity range of (21) lies within the elasticity range of samples.

The implementation of the strain amplification concept does not introduce any additional parameters into the model. It applies to microstretches and does not contradict the incompressibility constraint valid for the macroscale deformations. Indeed, this constraint is a purely macroscopic phenomenon and does not necessarily hold for microscopic deformations.

3.3. Macroscale behavior. Now, the total strain energy of the rubber matrix is given in (19). The constitutive equation for the first Piola–Kirchhoff stress tensor \mathbf{P} can be written as

$$\mathbf{P} = \frac{\partial \Psi_M}{\partial \mathbf{F}} = \frac{\partial \Psi_{pp}}{\partial \mathbf{F}} + \frac{\partial \Psi_{cc}}{\partial \mathbf{F}}, \quad (25)$$

where

$$\begin{aligned} \frac{\partial \Psi_{cc}}{\partial \mathbf{F}} &= \sum_{i=1}^k N_c w_i \frac{\partial \psi(n_c, x)}{\partial x} \bigg|_{x=\chi} \frac{1}{2\chi} \frac{\partial \mathbf{D}_i \bar{\mathbf{C}} \mathbf{D}_i}{\partial \bar{\mathbf{F}}} : \frac{\partial \bar{\mathbf{F}}}{\partial \mathbf{F}}, \\ \frac{\partial \Psi_{pp}}{\partial \mathbf{F}} &= \sum_{i=1}^k w_i \frac{\partial \Psi}{\partial \lambda} \frac{\partial \lambda}{\partial \chi} \frac{1}{2\chi} \frac{\partial \mathbf{D}_i \bar{\mathbf{C}} \mathbf{D}_i}{\partial \bar{\mathbf{F}}} : \frac{\partial \bar{\mathbf{F}}}{\partial \mathbf{F}}. \end{aligned} \quad (26)$$

These equations can be further simplified by means of the following identities:

$$\frac{\partial \psi_c(n, x \bar{R})}{\partial x} = \frac{1}{a} \bar{R} K T \mathcal{L}^{-1} \left(\frac{x \bar{R}}{a b n} \right), \tag{27}$$

$$\frac{\partial \psi(n, x)}{\partial x} = \sqrt{b n} K T \mathcal{L}^{-1} \left(\frac{x}{\sqrt{b n}} \right), \tag{28}$$

$$\frac{\partial \Psi}{\partial \lambda} = N_0 \Phi(\lambda_m) \int_{D_A(\lambda_m)} \hat{P}(n) \frac{\partial \psi_c(n, x \bar{R})}{\partial x} \Big|_{x=\lambda} dn, \tag{29}$$

$$\frac{\partial \lambda}{\partial \chi} = \frac{1}{1 - C^p}, \tag{30}$$

$$\frac{\partial \mathbf{D} \bar{\mathbf{C}} \mathbf{D}}{\partial \bar{\mathbf{F}}} : \frac{\partial \bar{\mathbf{F}}}{\partial \mathbf{F}} = 2 \bar{\mathbf{F}} (\mathbf{D} \otimes \mathbf{D}) : J^{-1/3} \mathbb{1} = 2 J^{-1/3} \bar{\mathbf{F}} (\mathbf{D} \otimes \mathbf{D}). \tag{31}$$

Thus, (25) yields

$$\mathbf{P} = \sum_{i=1}^k (P_{cc}(\mathbf{D}_i) + P_{pp}(\mathbf{D}_i)) \frac{w_i}{\chi} J^{-1/3} \bar{\mathbf{F}}(\mathbf{D}_i \otimes \mathbf{D}_i), \tag{32}$$

where

$$P_{cc}(\mathbf{x}) = \tilde{N}_c \sqrt{b n_c} \mathcal{L}^{-1} \left(\frac{\tilde{\chi}}{\sqrt{b n_c}} \right), \tag{33}$$

$$P_{pp}(\mathbf{x}) = \frac{\bar{R}}{a} \frac{\tilde{N}_0}{1 - C^p} \Phi(\tilde{\lambda}_m) \int_{D_A(\tilde{\lambda}_m)} \hat{P}(n) \mathcal{L}^{-1} \left(\frac{\tilde{\chi} \bar{R}}{a b n} \right) dn. \tag{34}$$

A proper approximation approach for the inverse Langevin function can be chosen depending on the elongation range of polymer chains. In this study, the elongation ratio at which the chains are debonded from the aggregate surface is described by ν . Depending on its value, two different functions approximating the inverse Langevin function are utilized.

In cases of moderate and large deformations, Taylor expansion is more favorable (see [Itskov et al. 2012]). However, if chain breakage occurs very close to the fully stretched state of the chains $\nu < 1.04$, then Padé approximants [Puso 2003] show better agreement with the exact values. Accordingly

$$\mathcal{L}^{-1}(x) \cong \begin{cases} \sum_{i=0}^n C_i x^i & \text{if } \nu \geq 1.04, \\ \frac{3x}{1 - x^3} & \text{if } \nu < 1.04, \end{cases} \tag{35}$$

where the number of terms n and the values of C_i are given in [Itskov et al. 2012].

4. Thermodynamic consistency

Since the strain energy of the rubber matrix Ψ_M is influenced by a number of internal variables, namely λ_m , one can rewrite Ψ_M as

$$\Psi_M := \hat{\Psi}_M(\bar{\mathbf{C}}, \boldsymbol{\Omega}) = \tilde{\Psi}_M(\bar{\mathbf{F}}, \boldsymbol{\Omega}), \tag{36}$$

where

$$\Omega = \{\lambda_m^D : \mathbf{D} \in \mathbb{V}^3 \wedge |\mathbf{D}| = 1\}. \tag{37}$$

Accordingly, the Clausius–Duhem inequality resulting from the second law of thermodynamics can be reduced to

$$-\partial_{\lambda_m^D} \Psi_M \cdot \dot{\lambda}_m^D \geq 0 \quad \text{for all } \mathbf{D}. \tag{38}$$

Under unloading and reloading $\dot{\lambda}_m^D = 0$ while $\lambda_m^D > 0$ in primary loading. Thus, the Clausius–Duhem inequality is satisfied if during the primary loading, the following inequality:

$$\frac{\partial \Psi_M}{\partial \lambda_m^D} \leq 0 \quad \text{for all } \mathbf{D} \tag{39}$$

holds. With respect to (7) and (18), (38) yields

$$\frac{\partial \Psi}{\partial \lambda_m^D} \leq 0 \quad \text{for all } \mathbf{D}. \tag{40}$$

We will prove (40) for an arbitrary direction \mathbf{D} and for the sake of brevity denote λ_m^D by x . Using (16) we further obtain

$$\frac{d\Phi(x)}{dx} \int_{n_{c-f}(x)}^{n_{\max}} \hat{P}(n) \psi_c(n, \lambda \bar{R}) \, dn - \frac{dn_{c-f}(x)}{dx} \Phi(x) \hat{P}(n_{c-f}(x)) \psi_c(n_{c-f}(x), \lambda \bar{R}) \leq 0, \tag{41}$$

where

$$\frac{d\Phi(x)}{dx} = -x \left(\frac{\nu \bar{R}}{ab} \right)^2 \Phi^2(x) \hat{P}(n_{c-f}(x)). \tag{42}$$

Since (41) should be verified just during the primary loading ($\dot{\lambda}_m^D = \dot{\lambda}$), it can be rewritten as

$$n_{c-f}(x) \left(\int_{n_{c-f}(x)}^{n_{\max}} \hat{P}(n) \psi_c(n, \lambda \bar{R}) \, dn \right) - \left(\int_{n_{c-f}(x)}^{n_{\max}} \hat{P}(n) n \, dn \right) \psi_c(n_{c-f}(x), \lambda \bar{R}) \leq 0, \tag{43}$$

which holds since, in view of (2), we have the following inequalities:

$$n_{c-f}(x) \leq n \quad \text{for all } n \in \{n_{c-f}(x), n_{\max}\}, \quad \text{hence} \quad n_{c-f}(x) < \int_{n_{c-f}(x)}^{n_{\max}} \hat{P}(n) n \, dn;$$

and

$$\psi_c(n_{c-f}(x), x \bar{R}) \geq \psi_c(n, x \bar{R}) \quad \text{for all } n \in \{n_{c-f}(x), n_{\max}\},$$

hence

$$\int_{n_{c-f}(x)}^{n_{\max}} \hat{P}(n) \psi_c(n, x \bar{R}) \, dn < \psi_c(n_{c-f}(x), x \bar{R}).$$

5. Finite element linearization

In the following we derive the tangent tensor defined by

$$\mathbb{C} = 2 \frac{\partial \mathbf{S}}{\partial \mathbf{C}}, \tag{44}$$

where \mathbf{S} denotes the second Piola–Kirchhoff stress tensor. By using the fourth-order deviatoric projection tensor in the Lagrangian description

$$\mathbb{P}_{\text{Dev}} = \mathbb{I}^s - \frac{1}{3} \mathbf{C}^{-1} \odot \mathbf{C}, \tag{45}$$

for a nearly incompressible material \mathbf{S} is formulated as

$$\mathbf{S} = 2 \frac{\partial \Psi_N(\mathbf{C}, \Omega)}{\partial \mathbf{C}} = 2 \frac{\partial \Psi_M}{\partial \bar{\mathbf{C}}} : \frac{\partial \bar{\mathbf{C}}}{\partial \mathbf{C}} + 2 \frac{\partial U}{\partial J} \frac{\partial J}{\partial \mathbf{C}} = \underbrace{J^{-2/3} (\mathbb{P}_{\text{Dev}} : \bar{\mathbf{S}})}_{\mathbf{S}^{\text{iso}}} + \underbrace{U' J \mathbf{C}^{-1}}_{\mathbf{S}^{\text{vol}}}, \quad (46)$$

where $\bar{\mathbf{S}} = 2 \partial \Psi_M / \partial \bar{\mathbf{C}}$.

Accordingly, the tangent tensor of the rubber matrix is given by

$$\mathbb{C} = 2 \frac{\partial \mathbf{S}}{\partial \mathbf{C}} = 2 \underbrace{\frac{\partial \mathbf{S}^{\text{iso}}}{\partial \mathbf{C}}}_{\mathbb{C}^{\text{iso}}} + 2 \underbrace{\frac{\partial \mathbf{S}^{\text{vol}}}{\partial \mathbf{C}}}_{\mathbb{C}^{\text{vol}}}. \quad (47)$$

Substituting (46) into (47) gives

$$\mathbb{C}^{\text{iso}} = J^{-4/3} \mathbb{P}_{\text{Dev}} : \bar{\mathbf{C}} : \mathbb{P}_{\text{Dev}}^T - \frac{2}{3} J^{-2/3} [\mathbf{C}^{-1} \odot \bar{\mathbf{S}} + \bar{\mathbf{S}} \odot \mathbf{C}^{-1}] + \frac{2}{3} (\bar{\mathbf{S}} : \bar{\mathbf{C}}) \mathbb{Z}, \quad (48)$$

$$\mathbb{C}^{\text{vol}} = J(U'' J + \frac{5}{3} U') \mathbf{C}^{-1} \odot \mathbf{C}^{-1} - 2U' J \mathbb{Z}, \quad (49)$$

where the fourth-order tensor products are defined in [Itskov 2009].

Finally, the tangent tensor is obtained in view of (47) as

$$\begin{aligned} \mathbb{C} = J^{-4/3} \mathbb{P}_{\text{Dev}} : \bar{\mathbf{C}} : \mathbb{P}_{\text{Dev}}^T - \frac{2}{3} J^{-2/3} (\mathbf{C}^{-1} \odot \bar{\mathbf{S}} + \bar{\mathbf{S}} \odot \mathbf{C}^{-1}) \\ + \frac{2}{3} (\bar{\mathbf{S}} : \bar{\mathbf{C}} - 3U' J) \mathbb{Z} + J(U'' J + \frac{5}{3} U') \mathbf{C}^{-1} \odot \mathbf{C}^{-1}, \end{aligned} \quad (50)$$

where $\mathbb{Z} = [\frac{1}{3} \mathbf{C}^{-1} \odot \mathbf{C}^{-1} + (\mathbf{C}^{-1} \otimes \mathbf{C}^{-1})^s]$ and $\bar{\mathbf{C}}$ is given by (see details in the Appendix)

$$\bar{\mathbf{C}} = 2 \frac{\partial \bar{\mathbf{S}}}{\partial \bar{\mathbf{C}}} + 2 \sum_{i=1}^k \frac{\partial \bar{\mathbf{S}}(\bar{\mathbf{C}}, \Omega)}{\partial \lambda_m^{d_i}} \odot \frac{\partial \lambda_m^{d_i}}{\partial \bar{\mathbf{C}}}. \quad (51)$$

6. Experiment

The experimental study¹ presented here consists of three parts: loading in two orthogonal directions to capture induced anisotropy, multiaxial tension tests to evaluate model accuracy, and cyclic tension tests on a compound with different filler concentrations to investigate the influence of material parameters.

6.1. Loading in two orthogonal directions. In this experiment we used a cross-shaped specimen (Figure 2) made of 50 phr carbon black filled polychloroprene rubber (CR). The exact composition of the elastomer used in this experiment is given in Table 1. The experiment was performed at room temperature with a strain rate of 40% /min.

The four arms of the cross-shaped specimens have multiple slits parallel to the sides to obtain a nearly homogeneous state of uniaxial tension in the measurement area (see, for example, [Pawelski 2001]). The specimens were loaded by a spindle-driven two-pillar universal tensile test machine. The machine provides a constant clamping force, which is important for measurement reproducibility [Itskov et al. 2006]. Fast clamping and unclamping procedures furthermore reduced the influence of time-dependent

¹The experimental part of this work is a result of cooperation with Professor E. Haberstroh (Institute of Rubber Technology, RWTH Aachen University) whose contribution is gratefully acknowledged.

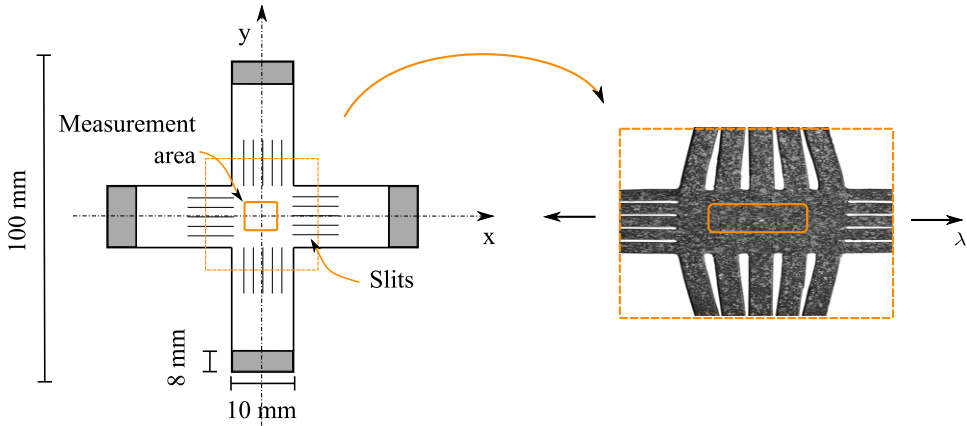


Figure 2. A cross-shaped specimen in its virgin and deformed states. The measurement area retains its rectangular form, which implies a homogeneous strain distribution there.

effects such as relaxation. Using an optical measuring system, stretches in the measurement area were evaluated by a noncontact method.

The experimental procedure was as follows: the virgin specimen was subjected to loading-unloading cycles of uniaxial tension (in the x -direction) with increasing stretch amplitudes of 1.15, 1.30, 1.45, 1.60, and 1.75. Five cycles were conducted for each stretch amplitude.

After unloading to the stress-free state, the sample was unclamped and reclamped for consequent loading in the orthogonal direction (the y -direction). Despite resulting residual strains from the previous loading cycles, the new configuration is considered as the reference configuration for the loading in the y -direction. The above-described loading procedure was repeated again in the y -direction.

The nominal stress P is plotted versus stretch χ in Figure 3a. Under tension in the x -direction, the classical Mullins effect and permanent set can be seen after the first loading cycle. Under tension in the y -direction, the strong anisotropy of the Mullins effect can be observed.

In order to resume the ideal Mullins effect, the hysteresis observed in the second and subsequent cycles is eliminated from the experimental data. Accordingly, Figure 3b illustrates the idealized Mullins effect, permanent set, and induced anisotropy.

Compound	phr	Density (kg/m ³)
Polychloroprene (CR)	100	1210
Carbon black (N330)	50	1800
Antioxidant	2	990
Processing aids	1.5	1230
Activator	2	3600
Cross-linker	5	2000
Plasticizer	2	970

Table 1. Compound specifications of the rubber sample used for the cross-shaped specimen.

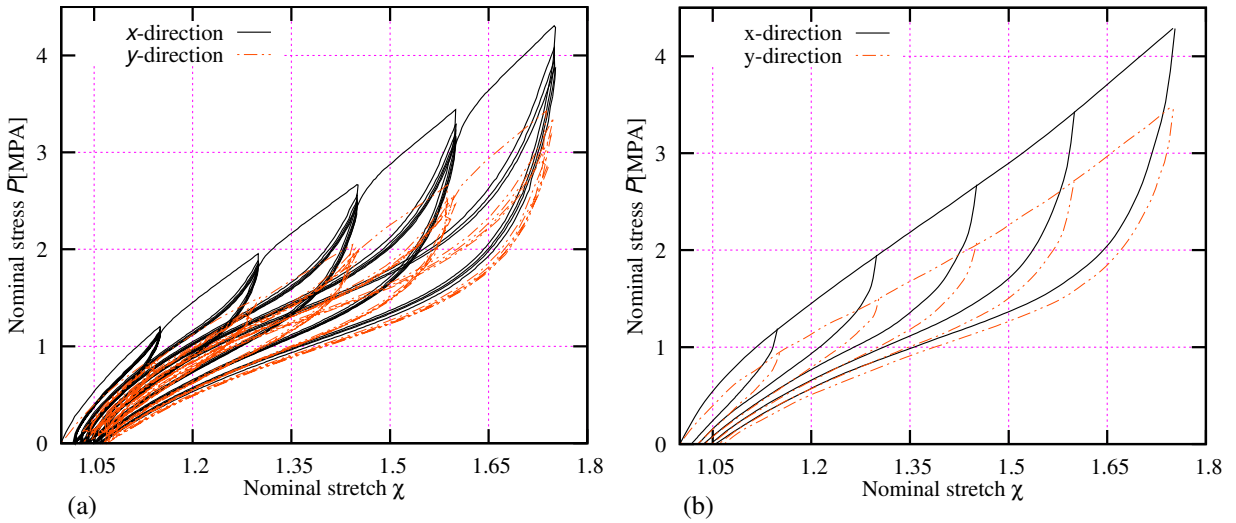


Figure 3. (a) Initial and (b) treated experimental results of the uniaxial tension test of the cross-shaped specimen in the two orthogonal directions.

6.2. Multiaxial tension test. To investigate the evolution of the deformation-induced anisotropy, its magnitude was studied by loading in different directions, in the following experiment.

A large specimen was elongated up to a certain stretch level then unloaded (one complete uniaxial tension cycle). Then, a small dumbbell-shaped specimen was cut from the prestretched specimen at an angle Φ inclined to the initial tension direction, with $\Phi = 0^\circ, 15^\circ, 22.5^\circ, 45^\circ, 67.5^\circ, 90^\circ$ (see Figure 4). The small samples were then loaded up to the same stretch level as the large sample and then unloaded.

Using this approach, one can study the mechanical response of the material in different directions. The comparison of the responses of the large and small specimens for $\Phi = 0^\circ$ is shown in Figure 5.

The samples were made of 50 phr (24% by volume) carbon black filled polychloroprene rubber (CR) with the composition given in Table 2. The mechanical responses of the small samples for different

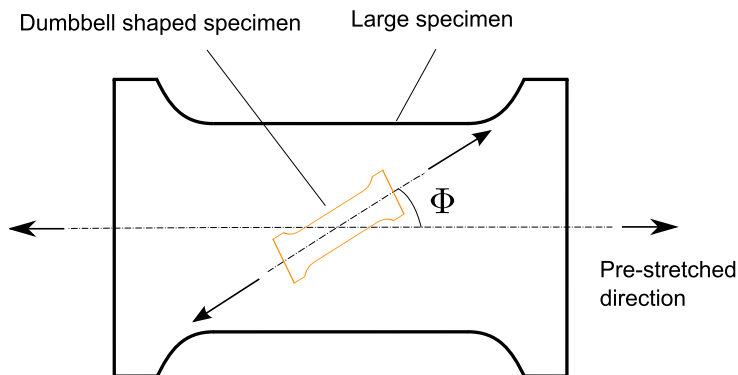


Figure 4. Sample preparation for multiaxial tension test. Small samples were cut under a certain angle Φ to the prestretch direction of the large sample.

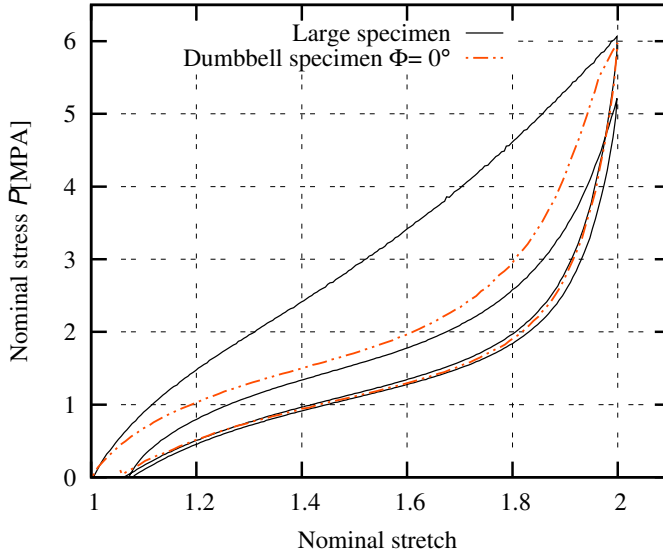


Figure 5. The mechanical response of the large sample in comparison with the smaller one.

Compound	phr	Density (kg/m ³)
Polychloroprene (CR)	100	1210
Carbon black (N330)	50	1800
Antioxidant	1	990
Processing aids	4	1230
Activator	1	3600
Cross-linker	5	2000
Plasticizer	10	970

Table 2. Compound specifications of the rubber sample used in the multiaxial experiment.

directions are depicted in [Figure 6](#). One observes that the Mullins effect decreases with increasing angle Φ .

6.3. Influence of the filler concentration. It is expected that stress softening increases in compounds with higher filler concentrations. In this experiment, a compound with three different filler concentrations was used. The ingredients of the compound are given in [Table 2](#), and the filler concentrations are 20, 40, and 60 phr (11, 20, and 28% by volume). The transverse loading experiment described in [Section 6.1](#) is then applied to each sample. The results plotted in [Figure 7](#) confirm that the Mullins effect, permanent set, and hysteresis are more pronounced in samples with higher filler concentrations.

7. Comparison with experimental results

The objective of this section is to assess the predictive capabilities of the proposed constitutive model by comparing it with the experimental data presented in [Section 6](#).

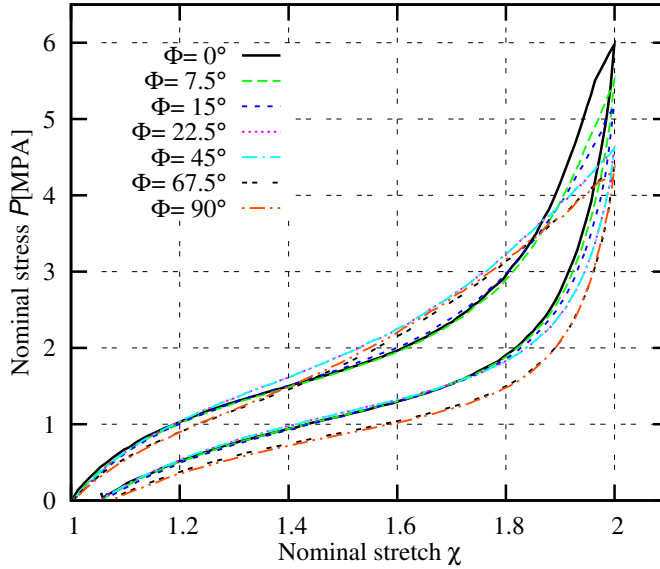


Figure 6. Experimental results of uniaxial tensile tests on small samples cut under different angles Φ from the large sample.

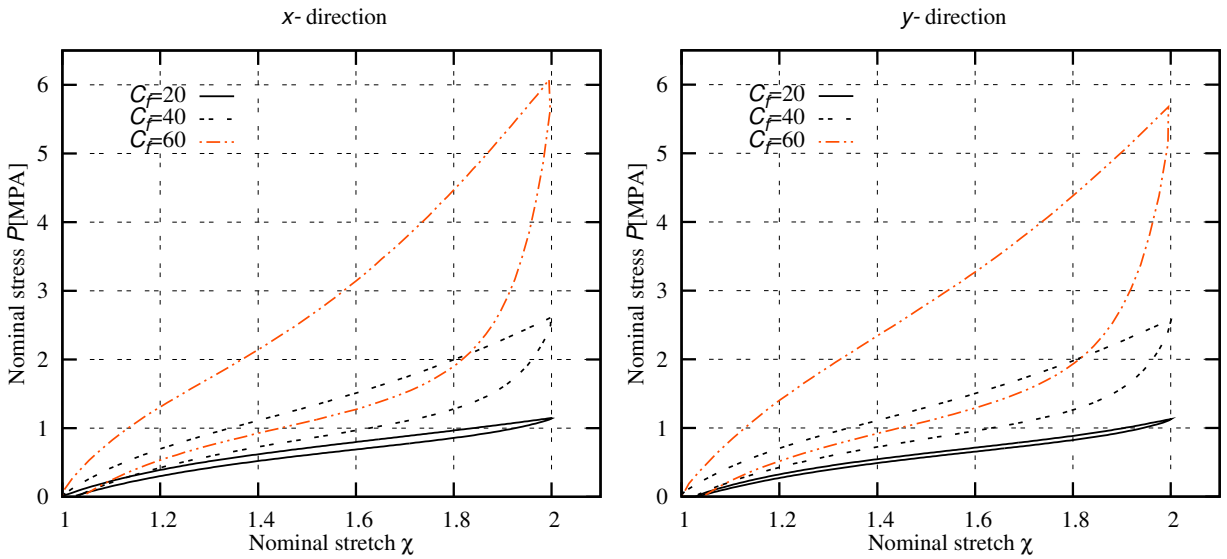


Figure 7. Experimental results of the uniaxial deformation of samples with different filler concentrations in the (left) x and (right) y -directions.

7.1. Transverse loading. By means of seven material parameters, the model was fitted to the transverse loading experimental data presented in Section 6.1. To this end, the least-square error function was minimized with the aid of the Levenberg–Marquardt algorithm. The obtained values of the material parameters are given in Table 3, while the predicted stress-stretch curves are plotted in Figure 8 against the experimental diagrams for the x and y -directions.

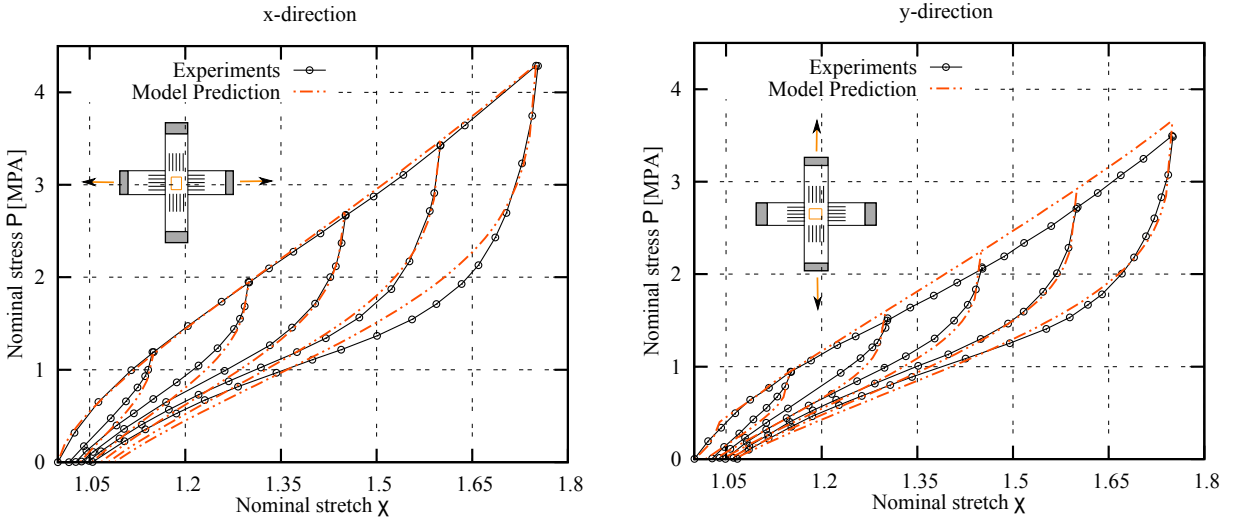


Figure 8. Comparison of the nominal stress-stretch curves of the model and the experiment for the uniaxial tension test in the (left) x and (right) y -directions.

κ	ν	\bar{R}	n_{\max}	n_c	\tilde{N}_0 (MPa)	\tilde{N}_c (MPa)
14.824	1.0065	6.406	24.9135	100	2.8356	1.8141

Table 3. Parameters of the network evolution model for 50 phr CR used in the transverse loading experiment.

κ	ν	\bar{R}	n_{\max}	n_c	\tilde{N}_0 (MPa)	\tilde{N}_c (MPa)
4.218	1.0057	5.558	26.425	100	6.722	1.167

Table 4. Parameters of the network evolution model for 50 phr CR used in the multiaxial loading experiment.

The loading-unloading cycle of the 1.6 stretch amplitude in the x -direction was used for the fitting. Thus, good agreement with other unloading curves in the x -direction and all loading-unloading curves in the y -direction was obtained automatically.

7.2. Multiaxial tension test. In the multiaxial tension test, the residual stretches in the small samples were taken into account in their new reference configurations.

The material parameters given in Table 4 were obtained by fitting the model to the experimental data on the large sample. Then, using these parameters, the multiaxial loading experiment was simulated and compared to the experimental data as shown in Figure 9.

7.3. Influence of the filler concentration. The aim of this experiment was to check the capabilities of our model to simulate rubbers with different filler concentrations. To this end, samples made of the same compound and different filler concentrations were analyzed.

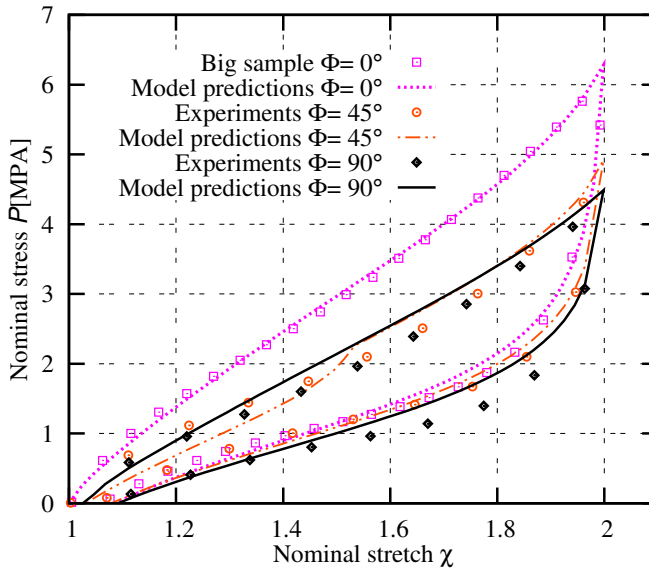


Figure 9. Comparison of the model predictions with the experimental results for the $\Phi = 0^\circ, 45^\circ, 90^\circ$ small samples.

C_f (phr)	κ	ν	\bar{R}	n_{\max}	n_c	\tilde{N}_0 (MPa)	\tilde{N}_c (MPa)
60	1.6203	1.0050	4.8700	24.7144	100	8.5121	1.0372
40	0.8094	1.0050	5.6747	38.7337	100	8.5121	1.0372
20	0.002552	1.0050	6.7090	97.1366	100	8.5121	1.0372

Table 5. Parameters of the network evolution model for fitting to compounds with different filler concentrations. Constant material parameters are shaded.

Since the sample materials differed from each other just in filler concentration, the material parameters independent of the filler concentration should remain constant for all simulations.

To verify this concept, we first calculated the seven material parameters of the model by fitting to the uniaxial loading result of 60 phr CR in the x -direction (see Table 5). Then, the model simulations were compared to the experimental results for this material in the x and y -directions (see Figure 10).

The parameters $\{\kappa, R, n_{\max}\}$ are directly influenced by the concentration of filler and ν by the type of filler. The parameters $\{n_c, \tilde{N}_0, \tilde{N}_c\}$ highly depend on the cross-linking and monomer properties, which are constant in the three samples. In addition, the number of active segments in a network, namely $\{\tilde{N}_0, \tilde{N}_c\}$, slightly changes with the filler concentration due to the immobilization of some segments around the aggregates, which are generally referred to as bound rubber. However, by excluding the effect of the bound rubber, the parameters $\{\nu, n_c, \tilde{N}_0, \tilde{N}_c\}$ can be assumed to be independent of the filler concentration.

In the next step, simulating the behavior of 40 and 20 phr CR, the material parameters $\{\nu, n_c, \tilde{N}_0, \tilde{N}_c\}$ were taken from the fitting to 60 phr CR experimental data, and the rest, $\{\kappa, R, n_{\max}\}$, approximated by phenomenological relations which take the forms of power functions in terms of the filler concentration.

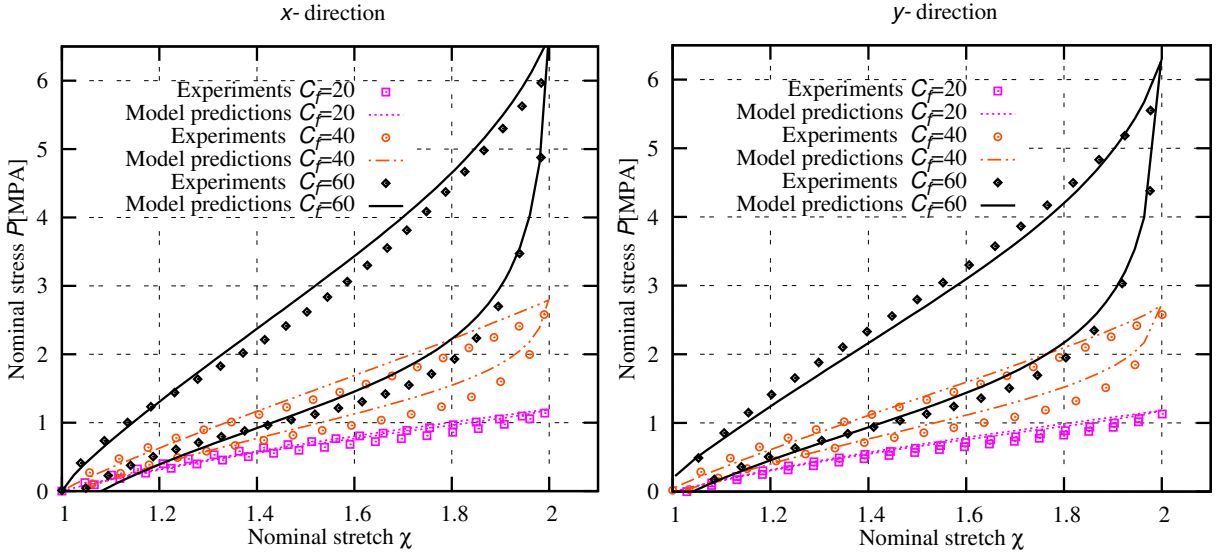


Figure 10. Comparison of the model predictions with the experimental results of samples with different filler concentrations. A transverse loading experiment is applied to each sample and the results in the (left) x and (right) y -directions are compared.

Despite the error induced by neglecting the effect of bound rubber, the predictions of the model using the aforementioned set of parameters show relatively good agreement with experimental results (see Figure 10). This further suggests that the changes in material parameters for different filler concentrations can be obtained by performing only one fitting procedure and enables one to simulate rubbers of the same compound with various filler concentrations based on only one set of fitting parameters.

8. Application examples

In this section, our model, implemented into the commercial FE code ABAQUS, is illustrated by two examples with large inhomogeneous deformations. First, the behavior of a thin rubber sheet with a hole in the middle is simulated and compared with experimental results under uniaxial tension. In the second test, the model predicts the behavior of an industrial damper under cyclic loading.

8.1. Rectangular rubber specimen with a central hole under uniaxial tension. The objective of this experiment is to assess the accuracy of the proposed constitutive model in predicting complex strain fields.

The specimen is made of a 60 phr carbon black filled rubber, with the exact compound given in Table 5. It has a rectangular shape ($100 \times 35 \times 2$ mm) with a hole of $D = 14$ mm at its center (see Figure 11). The hole was punched out by a mechanical cutting device.

The experiment is performed at room temperature with a strain rate of $\dot{\epsilon} = 0.4$ /s and stretch amplitude of $\epsilon = 0.75$. The strain field on the surface of the specimen is accurately measured by an optical measuring system (GOM Aramis), where the displacements of several points on the sample are captured and a detailed displacement field is provided.

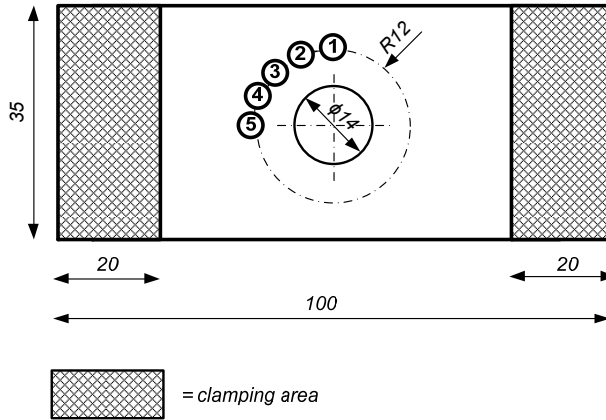


Figure 11. Shape of the test specimen.

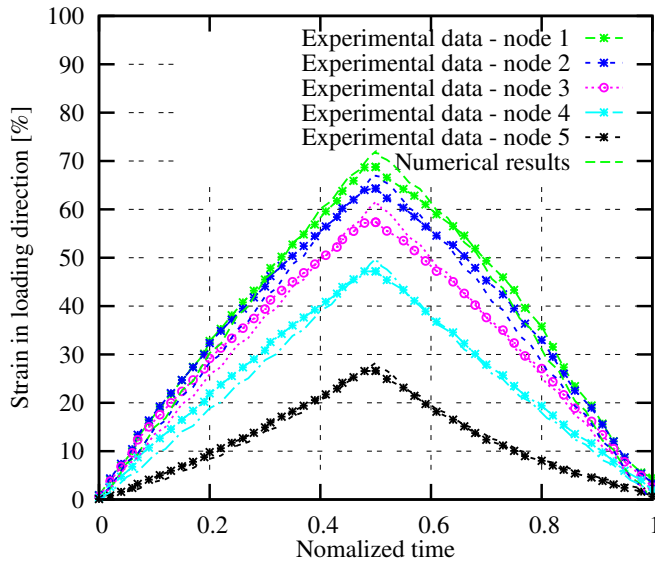


Figure 12. Comparison between strains in the loading direction from the FE results and the experimental data.

Five points on the specimen surface are chosen, as shown in Figure 11. Strains at these points are compared with the numerical results of the model simulations with 922 cubic elements. Good agreement between the experimental data and the numerical simulation is observed (see Figure 12).

8.2. Rubber suspension system. In another example, the model is used to simulate the behavior of a rubber component in an industrial application. To this end, cyclic loading of a cylindrical rubber string², shown in Figure 13, is simulated and compared with the measured data. The specimen is part of a suspension unit that is generally used as an impact stop, oscillation damper, or pivot bearing in machine constructions. The housing and the shaft of the bearing are made of steel. The string is made of carbon

²The samples used in this experiment are manufactured and provided by ROSTA AG.

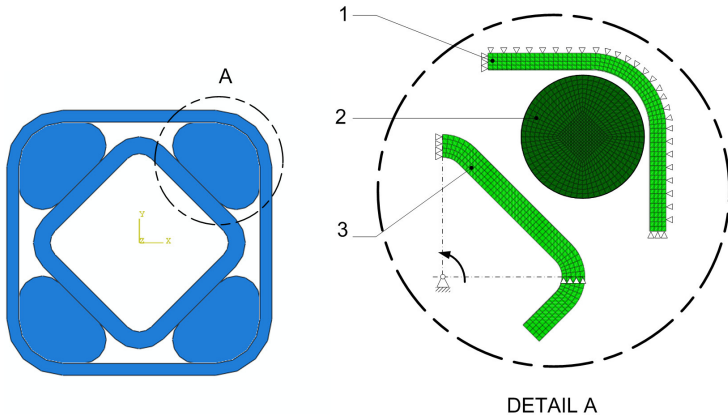


Figure 13. Assembled rubber suspension unit with housing (1), string (2), and shaft (3).

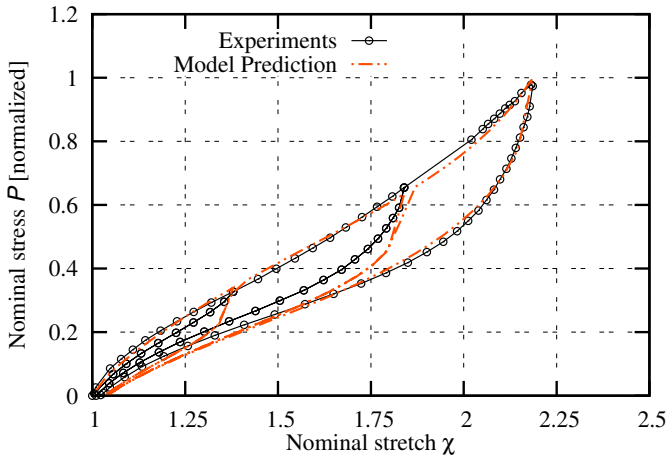


Figure 14. Comparison of the model predictions with the experimental results for the material of the string.

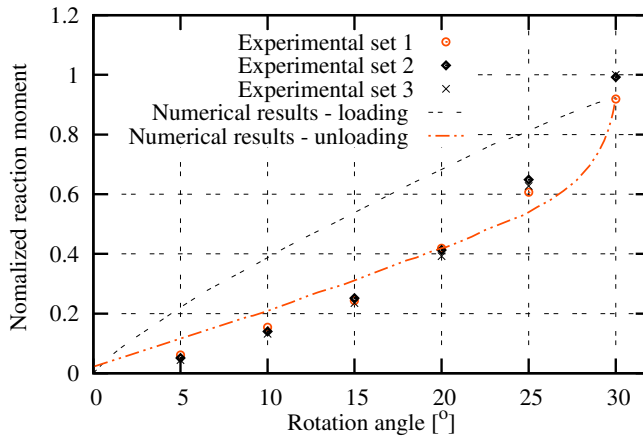


Figure 15. Comparison of the reaction moment at the center axis of the shaft for the FE results and the experiment.

black filled rubber with material constants obtained by fitting to the experimental data provided by the manufacturer, ROSTA AG (Figure 14).

Due to the symmetry of the structure, appropriate boundary conditions were applied to one-quarter of the rubber suspension unit, which was discretized by 2094 linear cubic elements. The simulation of the rubber suspension unit started with the assembly process from undeformed state (Figure 13), following by rotation of the shaft inside the bearing.

In Figure 15, the model predictions for the moment normalized with respect to the length of the string are plotted versus the angle and compared with the experimental data for the reaction moment. This was measured after five loading-unloading cycles, which corresponds to the unloading curve of our model. This curve demonstrates good agreement with the above-mentioned experimental data (see Figure 15).

9. Concluding remarks

The previously proposed network evolution model for carbon black filled rubbers exhibiting anisotropic Mullins effect is implemented here for finite elements simulations. To this end, the tangent moduli for elastic and nonelastic regimes are formulated in terms of internal variables. Additionally, the thermodynamical consistency of the model is proved.

In the next part, the concepts and predictive capabilities of the model are validated experimentally. The performance of the model is illustrated by comparing it to different sets of experimental data particularly designed to reveal the anisotropic Mullins effect and permanent set. Next, the predictive capabilities of the model are verified by comparing compounds with different filler concentrations. The model is also implemented into the FEM commercial code ABAQUS and its predictions for complex loading and geometrical problems are compared with the experimental data.

Everywhere, the model illustrated very good agreement with the experimental data. This fact, in addition to the simplicity of the proposed model, makes it a suitable option for commercial and industrial applications.

Appendix: Derivation of tangent tensors

In view of (36), the second Piola–Kirchhoff stress tensor $\bar{\mathbf{S}}$ is a nonlinear tensor valued-tensor function of state variables $\bar{\mathbf{C}}$ and Ω , defined as follows:

$$\bar{\mathbf{S}}(\bar{\mathbf{C}}, \Omega) = 2 \frac{\partial \hat{\Psi}_M(\bar{\mathbf{C}}, \Omega)}{\partial \bar{\mathbf{C}}} = 2 \frac{\partial \Psi_{cc}}{\partial \bar{\mathbf{C}}} + 2 \frac{\partial \Psi_{pp}}{\partial \bar{\mathbf{C}}} = \bar{\mathbf{S}}_{cc} + \bar{\mathbf{S}}_{pp}. \quad (\text{A.1})$$

Accordingly, in view of (27) one has

$$\begin{aligned} \bar{\mathbf{S}}_{cc} &= 2 \frac{\partial \Psi_{cc}}{\partial \bar{\mathbf{C}}} = \sum_{i=1}^k w_i \tilde{N}_c \sqrt{bn_c} \mathcal{L}^{-1} \left(\frac{\frac{D_i}{\chi}}{\sqrt{bn_c}} \right) \frac{1}{D_i} (\mathbf{D}_i \otimes \mathbf{D}_i), \\ \bar{\mathbf{S}}_{pp} &= 2 \frac{\partial \Psi_{pp}}{\partial \bar{\mathbf{C}}} = \sum_{i=1}^k w_i \tilde{N}_0 \Phi(\lambda_m) \frac{\mu \xi_i}{D_i} (\mathbf{D}_i \otimes \mathbf{D}_i), \end{aligned} \quad (\text{A.2})$$

where $\mu = \frac{1}{1-C^p}$. Furthermore, the parameter ξ_i is defined by

$$\xi_i = \frac{\bar{R}}{a} \int_{D_A(\lambda_m)}^{D_i} \hat{P}(n) \mathcal{L}^{-1} \left(\frac{\lambda \bar{R}}{abn} \right) dn. \quad (\text{A.3})$$

The standard Newton–Raphson procedure in finite element analysis requires a linearization of the relation between the second Piola–Kirchhoff stress tensor $\bar{\mathbf{S}}$ and the state variables $\bar{\mathbf{C}}$ and Ω . The modified tangent tensor $\bar{\mathbb{C}}$ is formulated by dropping the higher-order terms of the following Taylor expansion:

$$\begin{aligned} \bar{\mathbf{S}}(\bar{\mathbf{C}} + d\bar{\mathbf{C}}, \Omega + d\Omega) &= \bar{\mathbf{S}}(\bar{\mathbf{C}}, \Omega) + d\bar{\mathbf{S}} \\ &= \bar{\mathbf{S}}(\bar{\mathbf{C}}, \Omega) + \frac{\partial \bar{\mathbf{S}}(\bar{\mathbf{C}}, \Omega)}{\partial \bar{\mathbf{C}}} : d\bar{\mathbf{C}} + \sum_{i=1}^k \frac{\partial \bar{\mathbf{S}}(\bar{\mathbf{C}}, \Omega)}{\partial \lambda_m^{D_i}} d\lambda_m^{D_i} + \Theta(d\bar{\mathbf{C}}^2, d\lambda_m^{D_i 2}). \end{aligned}$$

Thus, the linearization process yields

$$\begin{aligned} d\bar{\mathbf{S}} &= \frac{\partial \bar{\mathbf{S}}(\bar{\mathbf{C}}, \Omega)}{\partial \bar{\mathbf{C}}} : d\bar{\mathbf{C}} + \sum_{i=1}^k \frac{\partial \bar{\mathbf{S}}(\bar{\mathbf{C}}, \Omega)}{\partial \lambda_m^{D_i}} d\lambda_m^{D_i} = \frac{\partial \bar{\mathbf{S}}(\bar{\mathbf{C}}, \Omega)}{\partial \bar{\mathbf{C}}} : d\bar{\mathbf{C}} + \sum_{i=1}^k \frac{\partial \bar{\mathbf{S}}(\bar{\mathbf{C}}, \Omega)}{\partial \lambda_m^{D_i}} \left(\frac{\partial \lambda_m^{D_i}}{\partial \bar{\mathbf{C}}} : d\bar{\mathbf{C}} \right) \\ &= 2 \left[\frac{\partial \bar{\mathbf{S}}(\bar{\mathbf{C}}, \Omega)}{\partial \bar{\mathbf{C}}} + \sum_{i=1}^k \frac{\partial \bar{\mathbf{S}}(\bar{\mathbf{C}}, \Omega)}{\partial \lambda_m^{D_i}} \odot \frac{\partial \lambda_m^{D_i}}{\partial \bar{\mathbf{C}}} \right] : \frac{1}{2} d\bar{\mathbf{C}}, \end{aligned} \quad (\text{A.4})$$

which finally gives $\bar{\mathbb{C}}$ as

$$\bar{\mathbb{C}} = 2 \frac{\partial \bar{\mathbf{S}}}{\partial \bar{\mathbf{C}}} + 2 \sum_{i=1}^k \frac{\partial \bar{\mathbf{S}}(\bar{\mathbf{C}}, \Omega)}{\partial \lambda_m^{D_i}} \odot \frac{\partial \lambda_m^{D_i}}{\partial \bar{\mathbf{C}}}. \quad (\text{A.5})$$

In view of (A.1) and (A.5), the first part of the tangent tensor is given by

$$2 \frac{\partial \bar{\mathbf{S}}}{\partial \bar{\mathbf{C}}} = 2 \frac{\partial \bar{\mathbf{S}}_{cc}}{\partial \bar{\mathbf{C}}} + 2 \frac{\partial \bar{\mathbf{S}}_{pp}}{\partial \bar{\mathbf{C}}} = \bar{\mathbb{C}}_{cc} + \bar{\mathbb{C}}_{pp}. \quad (\text{A.6})$$

Next, $\bar{\mathbb{C}}_{cc}$ is calculated by using (A.2) as

$$\begin{aligned} \bar{\mathbb{C}}_{cc} &= 2 \sum_{i=1}^k w_i \tilde{N}_c \sqrt{bn_c} (\mathbf{D}_i \otimes \mathbf{D}_i) \odot \frac{\partial}{\partial \chi} \left[\frac{1}{\chi} \mathcal{L}^{-1} \left(\frac{\chi^{D_i}}{\sqrt{bn_c}} \right) \right] \frac{\partial \chi^{D_i}}{\partial \bar{\mathbf{C}}} \\ &= \sum_{i=1}^k w_i \tilde{N}_c \Delta_i (\mathbf{D}_i \otimes \mathbf{D}_i) \odot (\mathbf{D}_i \otimes \mathbf{D}_i), \end{aligned} \quad (\text{A.7})$$

where the parameter Δ_i is written as

$$\Delta_i = -\frac{\sqrt{bn_c}}{\chi_i^3} \beta + \frac{1}{\chi_i^2} \frac{\beta^2 \sinh^2 \beta}{\sinh^2 \beta - \beta^2}, \quad (\text{A.8})$$

by knowing

$$\frac{d\mathcal{L}^{-1}(y)}{dy} = \frac{1}{d\mathcal{L}(\beta)/d\beta} = \frac{\beta^2 \sinh^2 \beta}{\sinh^2 \beta - \beta^2}.$$

Furthermore, with respect to (A.2), one has for $\bar{\mathbb{C}}_{pp}$:

$$\begin{aligned} \bar{\mathbb{C}}_{pp} &= 2 \sum_{i=1}^k w_i \tilde{N}_0 \mu \Phi^{D_i}(\lambda_m) (\mathbf{D}_i \otimes \mathbf{D}_i) \odot \frac{\partial}{\partial \bar{\mathbf{C}}} \left[\frac{\xi_i}{\chi} \right] \\ &= \sum_{i=1}^k w_i \tilde{N}_0 \mu \Phi^{D_i}(\lambda_m) \left[-\frac{\xi_i}{\chi^3} + \frac{\mu \gamma_i}{\chi^2} \right] (\mathbf{D}_i \otimes \mathbf{D}_i) \odot (\mathbf{D}_i \otimes \mathbf{D}_i), \end{aligned} \quad (\text{A.9})$$

where $\gamma_i = d\xi_i/d\lambda^{D_i}$.

Finally, (A.6) is simplified to

$$2 \frac{\partial \bar{\mathbf{S}}}{\partial \bar{\mathbf{C}}} = \sum_{i=1}^k w_i \left(\tilde{N}_c \Delta_i + \tilde{N}_0 \mu \Phi^{D_i}(\lambda_m) \left[-\frac{\xi_i}{\chi^3} + \frac{\mu \gamma_i}{\chi^2} \right] \right) \mathbb{D}_i, \quad (\text{A.10})$$

where $\mathbb{D}_i = (\mathbf{D}_i \otimes \mathbf{D}_i) \odot (\mathbf{D}_i \otimes \mathbf{D}_i)$.

For the second term of the tangent tensor, one has

$$\frac{\partial^{D_i} \lambda_m}{\partial \bar{\mathbf{C}}} = \begin{cases} \frac{\partial \lambda^{D_i}}{\partial \bar{\mathbf{C}}} = \frac{\mu}{2\chi} (\mathbf{D}_i \otimes \mathbf{D}_i), & \lambda^{D_i} = \lambda_m \text{ (in primary loading),} \\ \mathbf{0}, & \text{(in unloading or reloading),} \end{cases} \quad (\text{A.11})$$

which consequently gives

$$2 \sum_{i=1}^k \frac{\partial \bar{\mathbf{S}}(\bar{\mathbf{C}}, \Omega)}{\partial \lambda_m^{D_i}} \odot \frac{\partial^{D_i} \lambda_m}{\partial \bar{\mathbf{C}}} = 2 \sum_{i=1}^k \frac{\partial \bar{\mathbf{S}}(\bar{\mathbf{C}}, \Omega)}{\partial \lambda_m^{D_i}} \odot \frac{\mu}{2\chi} (\mathbf{D}_i \otimes \mathbf{D}_i) \delta(\mathbf{D}_i), \quad (\text{A.12})$$

where

$$\delta(\mathbf{D}_i) = \begin{cases} 1 & \text{if } \lambda^{D_i} = \lambda_m, \\ 0 & \text{if } \lambda^{D_i} \neq \lambda_m. \end{cases}$$

Since the second term of the tangent tensor is nonzero just in the case of primary loading, one obtains the following identity based on (A.2):

$$\begin{aligned} \frac{\partial \bar{\mathbf{S}}(\bar{\mathbf{C}}, \Omega)}{\partial \lambda_m^{D_i}} &= \frac{\partial \bar{\mathbf{S}}_{cc}}{\partial \lambda_m^{D_i}} + \frac{\partial \bar{\mathbf{S}}_{pp}}{\partial \lambda_m^{D_i}} = \frac{\partial}{\partial \lambda_m^{D_i}} \left(w_i \tilde{N}_0 \Phi^{D_i}(\lambda_m) \frac{\mu \xi_i}{\chi} (\mathbf{D}_i \otimes \mathbf{D}_i) \right) \\ &= w_i \tilde{N}_0 \frac{\mu}{\chi} (\mathbf{D}_i \otimes \mathbf{D}_i) \left[\Phi^{D_i}(\lambda_m) \frac{\partial \xi_i}{\partial \lambda_m^{D_i}} + \xi_i \frac{\partial \Phi^{D_i}(\lambda_m)}{\partial \lambda_m^{D_i}} \right]. \end{aligned} \quad (\text{A.13})$$

Next, substituting (42) and

$$\frac{\partial \xi_i}{\partial \lambda_m} = -\frac{\nu \bar{R}^2}{a^2 b} \hat{P}(n_{c-f}(\lambda_m)) \mathcal{L}^{-1}\left(\frac{1}{\nu}\right), \quad (\text{A.14})$$

into (A.13) gives

$$\frac{\partial \bar{\mathbf{S}}(\bar{\mathbf{C}}, \Omega)}{\partial \lambda_m} = w_i \tilde{N}_0 \Phi^{D_i}(\lambda_m) \eta_i \frac{1}{\chi} (\mathbf{D}_i \otimes \mathbf{D}_i), \quad (\text{A.15})$$

where

$$\eta_i = -\left(\frac{\nu \bar{R}}{ab}\right)^2 \hat{P}(n_{c-f}(\lambda_m)) \left[\frac{b}{\nu} \mathcal{L}^{-1}\left(\frac{1}{\nu}\right) + \xi_i \lambda_m \Phi^{D_i}(\lambda_m) \right]. \quad (\text{A.16})$$

Finally, the expanded formulation of the tangent tensor is obtained as

$$\bar{\mathbb{C}} = \sum_{i=1}^k w_i \left(\tilde{N}_c \Delta_i + \tilde{N}_o \mu \Phi^{D_i}(\lambda_m) \left[-\frac{\xi_i}{\chi^3} + \mu \frac{\gamma_i + \eta_i \delta(\mathbf{D}_i)}{\chi^2} \right] \right) \mathbb{D}_i. \quad (\text{A.17})$$

Acknowledgments

The authors thank the German Research Foundation (DFG) for their financial support of this work. The experimental part of this study is the result of cooperation with Professor E. Haberstroh (Institute of Rubber Technology, RWTH Aachen University) whose contribution is also gratefully acknowledged.

References

- [Aksel and Hübner 1996] N. Aksel and C. Hübner, “The influence of dewetting in filled elastomers on the changes of their mechanical properties”, *Arch. Appl. Mech.* **66**:4 (1996), 231–241.
- [Arruda and Boyce 1993] E. Arruda and M. Boyce, “A three-dimensional constitutive model for the large stretch behavior of rubber elastic materials”, *J. Mech. Phys. Solids* **41**:2 (1993), 389–412.
- [Beatty 2003] M. F. Beatty, “An average-stretch full-network model for rubber elasticity”, *J. Elasticity* **70**:1-3 (2003), 65–86.
- [Bergström and Boyce 1999] J. Bergström and M. Boyce, “Mechanical behavior of particle filled elastomers”, *Rubber Chem. Technol.* **72**:4 (1999), 633–656.
- [Bouasse and Carrière 1903] H. Bouasse and Z. Carrière, “Courbes de traction du caoutchouc vulcanisé”, *Ann. Fac. Sci. Toulouse (2)* **5**:3 (1903), 257–283.
- [Bueche 1960] F. Bueche, “Molecular basis for the Mullins effect”, *J. Appl. Polym. Sci.* **4**:10 (1960), 107–114.
- [Bueche 1961] F. Bueche, “Mullins effect and rubber-filler interaction”, *J. Appl. Polym. Sci.* **5**:15 (1961), 271–281.
- [Dargazany and Itskov 2009] R. Dargazany and M. Itskov, “A network evolution model for the anisotropic Mullins effect in carbon black filled rubbers”, *Int. J. Solids Struct.* **46**:16 (2009), 2967–2977.
- [Demirkoparan et al. 2009] H. Demirkoparan, T. J. Pence, and A. Wineman, “On dissolution and reassembly of filamentary reinforcing networks in hyperelastic materials”, *Proc. R. Soc. Lond. A* **465**:2103 (2009), 867–894.
- [Diani et al. 2006] J. Diani, M. Brieu, and J. Vacherand, “A damage directional constitutive model for Mullins effect with permanent set and induced anisotropy”, *Eur. J. Mech. A Solids* **25**:3 (2006), 483–496.
- [Diani et al. 2009] J. Diani, B. Fayolle, and P. Gilormini, “A review on the Mullins effect”, *Eur. Polym. J.* **45**:3 (2009), 601–612.
- [Dorfmann and Ogden 2004] A. Dorfmann and R. Ogden, “A constitutive model for the Mullins effect with permanent set in particle-reinforced rubber”, *Int. J. Solids Struct.* **41**:7 (2004), 1855–1878.
- [Drozdov and Dorfmann 2001] A. D. Drozdov and A. Dorfmann, “Stress-strain relations in finite viscoelastoplasticity of rigid-rod networks: applications to the Mullins effect”, *Contin. Mech. Therm.* **13**:3 (2001), 183–205.

- [Ehret et al. 2010] A. Ehret, M. Itskov, and H. Schmid, “Numerical integration on the sphere and its effect on the material symmetry of constitutive equations: a comparative study”, *Int. J. Numer. Methods Eng.* **81**:2 (2010), 189–206.
- [Elías-Zúñiga and Beatty 2002] A. Elías-Zúñiga and M. F. Beatty, “A new phenomenological model for stress-softening in elastomers”, *Z. Angew. Math. Phys.* **53**:5 (2002), 794–814.
- [Elías-Zúñiga and Rodríguez 2010] A. Elías-Zúñiga and C. A. Rodríguez, “A non-monotonous damage function to characterize stress-softening effects with permanent set during inflation and deflation of rubber balloons”, *Int. J. Eng. Sci.* **48**:12 (2010), 1937–1943.
- [Göktepe and Miehe 2005] S. Göktepe and C. Miehe, “A micro-macro approach to rubber-like materials, III: The micro-sphere model of anisotropic Mullins-type damage”, *J. Mech. Phys. Solids* **53**:10 (2005), 2259–2283.
- [Govindjee 1997] S. Govindjee, “An evaluation of strain amplification concepts via monte carlo simulations of an ideal composite”, *Rubber Chem. Technol.* **70**:1 (1997), 25–37.
- [Govindjee and Simo 1991] S. Govindjee and J. Simo, “A micro-mechanically based continuum damage model for carbon black-filled rubbers incorporating Mullins’ effect”, *J. Mech. Phys. Solids* **39**:1 (1991), 87–112.
- [Govindjee and Simo 1992] S. Govindjee and J. Simo, “Transition from micro-mechanics to computationally efficient phenomenology: carbon black filled rubbers incorporating Mullins effect”, *J. Mech. Phys. Solids* **40**:1 (1992), 213–233.
- [Hamed and Hatfield 1989] G. L. Hamed and S. Hatfield, “On the role of bound rubber in carbon-black reinforcement”, *Rubber Chem. Technol.* **62**:1 (1989), 143–156.
- [Hanson et al. 2005] D. Hanson, M. Hawley, R. Houlton, K. Chitanvis, P. Rae, E. Orler, and D. Wroblewski, “Stress softening experiments in silica-filled polydimethylsiloxane provide insight into a mechanism for the Mullins effect”, *Polymer* **46**:24 (2005), 10989–10995.
- [Heo and Xu 2001] S. Heo and Y. Xu, “Constructing fully symmetric cubature formulae for the sphere”, *Math. Comput.* **70**:233 (2001), 269–279.
- [Holt 1932] W. L. Holt, “Behavior of rubber under repeated stresses”, *Rubber Chem. Technol.* **5**:1 (1932), 79–89.
- [Holzapfel 2000] G. A. Holzapfel, *Nonlinear solid mechanics: a continuum approach for engineering*, Wiley, Chichester, 2000.
- [Houwink 1956] R. Houwink, “Slipping of molecules during the deformation of reinforced rubber”, *Rubber Chem. Technol.* **29**:3 (1956), 888–893.
- [Huntley et al. 1996] H. E. Huntley, A. S. Wineman, and K. R. Rajagopal, “Chemorheological relaxation, residual stress, and permanent set arising in radial deformation of elastomeric hollow spheres”, *Math. Mech. Solids* **1**:3 (1996), 267–299.
- [Itskov 2009] M. Itskov, *Tensor algebra and tensor analysis for engineers*, 2nd ed., Springer, Dordrecht, 2009.
- [Itskov et al. 2006] M. Itskov, E. Haberstroh, A. E. Ehret, and M. C. Vöhringer, “Experimental observation of the deformation induced anisotropy of the Mullins effect in rubber”, *Kautsch. Gummi Kunstst.* **59**:3 (2006), 93–96.
- [Itskov et al. 2012] M. Itskov, R. Dargazany, and K. Hörnes, “Taylor expansion of the inverse function with application to the Langevin function”, *Math. Mech. Solids* **17**:7 (2012), 693–701.
- [James and Guth 1943] H. James and E. Guth, “Theory of the elastic properties of rubbers”, *J. Chem. Phys.* **11**:10 (1943), 455–480.
- [Killian et al. 1994] H. G. Killian, M. Strauss, and D. W. Hamm, “Universal properties in filler-loaded rubbers”, *Rubber Chem. Technol.* **67**:1 (1994), 1–16.
- [Mark and Erman 2007] J. E. Mark and B. Erman, *Rubberlike elasticity: a molecular primer*, 2nd ed., Cambridge University Press, Cambridge, 2007.
- [Miehe and Keck 2000] C. Miehe and J. Keck, “Superimposed finite elastic-viscoelastic-plastoelastic stress response with damage in filled rubbery polymers: experiments”, *J. Mech. Phys. Solids* **48**:2 (2000), 323–365.
- [Mullins and Tobin 1957] L. Mullins and N. R. Tobin, “Theoretical model for the elastic behavior of filler-reinforced vulcanized rubbers”, *Rubber Chem. Technol.* **30**:2 (1957), 555–571.
- [Mullins and Tobin 1965] L. Mullins and N. R. Tobin, “Stress softening in rubber vulcanizates, I: Use of a strain amplification factor to describe the elastic behavior of filler-reinforced vulcanized rubber”, *J. Appl. Polym. Sci.* **9**:9 (1965), 2993–3009.

- [Pawelski 2001] H. Pawelski, “Softening behavior of elastomeric media after loading in changing directions”, pp. 27–36 in *Constitutive models for rubber, II: Proceedings of the Second European Conference (ECCMR)* (Hannover, 2001), edited by D. Besdo et al., Balkema, Lisse, 2001.
- [Puso 2003] M. Puso, *Mechanistic constitutive models for rubber elasticity and viscoelasticity*, Ph.D. thesis, University of California, Davis, CA, 2003, Available at <http://e-reports-ext.llnl.gov/pdf/243854.pdf>.
- [Rajagopal and Wineman 1992] K. R. Rajagopal and A. S. Wineman, “A constitutive equation for nonlinear solids which undergo deformation induced microstructural changes”, *Int. J. Plast.* **8**:4 (1992), 385–395.
- [Rault et al. 2006] J. Rault, J. Marchal, P. Judeinstein, and P. Albouy, “Stress-induced crystallization and reinforcement in filled natural rubbers: 2H NMR study”, *Macromolecules* **39**:24 (2006), 8356–8368.
- [Simo 1987] J. Simo, “On a fully three-dimensional finite-strain viscoelastic damage model: formulation and computational aspects”, *Comput. Methods Appl. Mech. Eng.* **60**:2 (1987), 153–173.
- [Treloar 2005] L. R. G. Treloar, *The physics of rubber elasticity*, 3rd ed., Oxford University Press, New York, 2005.
- [Wineman and Rajagopal 1990] A. S. Wineman and K. R. Rajagopal, “On a constitutive theory for materials undergoing microstructural changes”, *Arch. Mech. Stos.* **42**:1 (1990), 53–75.
- [Zimmermann and Wineman 2005] M. Zimmermann and A. Wineman, “On the elastic behavior of scission materials”, *Math. Mech. Solids* **10**:1 (2005), 63–88.

Received 12 Jun 2012. Revised 10 Oct 2012. Accepted 16 Oct 2012.

ROOZBEH DARGAZANY: roozbeh@mit.edu

Department of Materials Science and Engineering, Massachusetts Institute of Technology, 77 Massachusetts Avenue, Room 12002, Cambridge, MA 02139, United States

and

Department of Continuum Mechanics, RWTH Aachen University, Kackertstraße 9, 52072 Aachen, Germany

VU NGOC KHIÊM: vu@km.rwth-aachen.de

Department of Continuum Mechanics, RWTH Aachen University, Kackertstraße 9, 52072 Aachen, Germany

UWE NAVRATH: navrath@km.rwth-aachen.de

Department of Continuum Mechanics, RWTH Aachen University, Kackertstraße 9, 52072 Aachen, Germany

MIKHAIL ITSKOV: itskov@km.rwth-aachen.de

Department of Continuum Mechanics, RWTH Aachen University, Kackertstraße 9, 52072 Aachen, Germany

JOURNAL OF MECHANICS OF MATERIALS AND STRUCTURES

jomms.net

Founded by Charles R. Steele and Marie-Louise Steele

EDITORS

CHARLES R. STEELE Stanford University, USA
DAVIDE BIGONI University of Trento, Italy
IWONA JASIUK University of Illinois at Urbana-Champaign, USA
YASUHIKO SHINDO Tohoku University, Japan

EDITORIAL BOARD

H. D. BUI École Polytechnique, France
J. P. CARTER University of Sydney, Australia
R. M. CHRISTENSEN Stanford University, USA
G. M. L. GLADWELL University of Waterloo, Canada
D. H. HODGES Georgia Institute of Technology, USA
J. HUTCHINSON Harvard University, USA
C. HWU National Cheng Kung University, Taiwan
B. L. KARIHALOO University of Wales, UK
Y. Y. KIM Seoul National University, Republic of Korea
Z. MROZ Academy of Science, Poland
D. PAMPLONA Universidade Católica do Rio de Janeiro, Brazil
M. B. RUBIN Technion, Haifa, Israel
A. N. SHUPIKOV Ukrainian Academy of Sciences, Ukraine
T. TARNAI University Budapest, Hungary
F. Y. M. WAN University of California, Irvine, USA
P. WRIGGERS Universität Hannover, Germany
W. YANG Tsinghua University, China
F. ZIEGLER Technische Universität Wien, Austria

PRODUCTION production@msp.org

SILVIO LEVY Scientific Editor

Cover design: Alex Scorpan

See <http://jomms.net> for submission guidelines.

JoMMS (ISSN 1559-3959) is published in 10 issues a year. The subscription price for 2012 is US\$555/year for the electronic version, and \$735/year (+ \$60 shipping outside the US) for print and electronic. Subscriptions, requests for back issues, and changes of address should be sent to Mathematical Sciences Publishers, Department of Mathematics, University of California, Berkeley, CA 94720–3840.

JoMMS peer-review and production is managed by EditFLOW[®] from Mathematical Sciences Publishers.

PUBLISHED BY
 **mathematical sciences publishers**
<http://msp.org/>

A NON-PROFIT CORPORATION

Typeset in L^AT_EX

Copyright ©2012 by Mathematical Sciences Publishers

- A model for the shear displacement distribution of a flow line in the adiabatic shear band based on gradient-dependent plasticity**
XUE-BIN WANG and BING MA 735
- A pull-out model for perfectly bonded carbon nanotube in polymer composites**
KHONDAKER SAKIL AHMED and ANG KOK KENG 753
- A perfectly matched layer for peridynamics in two dimensions**
RAYMOND A. WILDMAN and GEORGE A. GAZONAS 765
- Displacement field in an elastic solid with mode-III crack and first-order surface effects**
TAMRAN H. LENGYEL and PETER SCHIAVONE 783
- On the choice of functions spaces in the limit analysis for masonry bodies**
MASSIMILIANO LUCCHESI, MIROSLAV ŠILHAVÝ and NICOLA ZANI 795
- Edge stiffness effects on thin-film laminated double glazing system dynamical behavior by the operational modal analysis**
ALI AKROUT, MARIEM MILADI CHAABANE, LOTFI HAMMAMI and MOHAMED HADDAR 837
- Network evolution model of anisotropic stress softening in filled rubber-like materials**
ROOZBEH DARGAZANY, VU NGOC KHIÊM, UWE NAVRATH and MIKHAIL ITSKOV 861